



## Research Article

# Microstructural evolution and energetic characteristics of TiZrHfTa<sub>0.7</sub>W<sub>0.3</sub> high-entropy alloy under high strain rates and its application in high-velocity penetration

WeiQi Tang<sup>a,b</sup>, Kun Zhang<sup>a,b,\*</sup>, Tianyu Chen<sup>a,b</sup>, Qiu Wang<sup>b,c</sup>, Bingchen Wei<sup>a,b,\*</sup>

<sup>a</sup> Key Laboratory of Microgravity (National Microgravity Laboratory), Institute of Mechanics, Chinese Academy of Sciences, Beijing 100190, China

<sup>b</sup> School of Engineering Science, University of Chinese Academy of Sciences, Beijing 100049, China

<sup>c</sup> State Key Laboratory of High Temperature Gas Dynamics, Institute of Mechanics, Chinese Academy of Sciences, Beijing 100190, China



## ARTICLE INFO

## Article history:

Received 10 March 2022

Revised 9 May 2022

Accepted 22 May 2022

Available online 27 June 2022

## Keywords:

Energetic structural materials

High-entropy alloys

Phase transformation

Ballistic tests

## ABSTRACT

Energetic structural materials (ESMs) integrated a high energy density and rapid energy release with the ability to serve as structural materials. Here, a novel triple-phase TiZrHfTa<sub>0.7</sub>W<sub>0.3</sub> high-entropy alloy (HEA) was fabricated and investigated as a potential ESM. A hierarchical microstructure was obtained with a main metastable body-centered-cubic (BCC) matrix with distributed Ta-W-rich BCC precipitates of various sizes and interwoven hexagonal close-packed (HCP) lamellar nano-plates. The compressive mechanical properties were tested across a range of strain rates and demonstrated a brittle-to-ductile transition as the strain rate increased while maintaining a high ultimate strength of approximately 2.5 GPa. This was due to the phase transformation from metastable matrix BCC to HCP structures. In addition, during the dynamic deformation, metal combustion originating from the failure surface was observed. Furthermore, the composition of the fragments was studied, and the results indicated that the addition of tungsten promoted combustion. Finally, the potential application of this HEA was evaluated by high-velocity penetration tests, and the results were compared to other typical structural materials for penetrators and bullets. A comparison was conducted by assessing the geometries of the penetration channel employing two dimensionless parameters normalized by the projectile size, representing longitudinal and lateral damage, respectively. The normalized depth of the TiZrHfTa<sub>0.7</sub>W<sub>0.3</sub> HEA projectile was comparable to those of the other investigated materials, but the normalized diameter was the largest, showing an excellent ability to deliver lateral damage.

© 2022 Published by Elsevier Ltd on behalf of The editorial office of Journal of Materials Science & Technology.

## 1. Introduction

Energetic structural materials (ESMs) are a special category of energetic materials that integrate high energy density and rapid energy release properties, as well as desirable mechanical properties [1–4]. They are expected to find applications in the defense sector as kinetic penetrators, reactive fragments, reactive bullets, reactive armor, and munition casings. ESMs can crush, self-react, or combust violently with air to rapidly release high amounts of energy under impact or penetration.

Contrary to traditional energetic materials such as explosives and propellants, ESMs should possess sufficient strength to ensure

their structural reliability and improve their penetration performance. They should also have higher reaction energy to result in greater lethality during a short detonation timescale. Usually, ESMs are inert under in-service conditions and insensitive to friction and heat, but they may undergo exothermic chemical reactions through extreme loading events such as high-velocity impact/penetration. Generally, based on the composition and reaction mechanisms, the conventional ESMs are categorized into thermite, intermetallic, metal-fluoropolymer systems and metastable intermixed composites [5,6]. Except for intermetallic, the other three types are actually mixtures, and their mechanical properties (strength or plasticity) are not sufficient to be used as structural materials. The current research for intermetallic mainly focuses on Ni-Al-based materials which are fabricated by the sintering process, and their mechanical properties are still not ideal for structural applications [5]. These alloys, such as W-Zr alloys, metallic glass composites,

\* Corresponding authors at: Institute of Mechanics, Chinese Academy of Sciences, Beijing 100190, China.

E-mail addresses: [zhangkun@imech.ac.cn](mailto:zhangkun@imech.ac.cn) (K. Zhang), [weibc@imech.ac.cn](mailto:weibc@imech.ac.cn) (B. Wei).

and multiple-phase high-entropy alloys (HEA), are ideal potential candidates for applications in the defense industry [7–9].

Although the mechanical response of ESMs has been studied for decades, the trade-off between their mechanical properties (strength, plasticity, etc.) and reactivity limits their applications ESMs, especially for multi-principle element alloys. For example, W-Zr alloys have been widely studied as high-strength ESMs, exhibiting a dual-phase BCC structure and good energetic release rate [10–13]. However, Wang et al. found that the W-Zr alloy is extremely susceptible to impact-induced reactions due to the brittleness of  $W_2Zr$  precipitates and may be broken further to react under the detonation pressure of warheads before colliding with a target, which could decrease their lethality [14]. To increase the lethality of W-Zr alloys, Xing et al. found that by increasing the composition of Ti, the coarsening of the brittle  $W_2Zr$  phase can be suppressed, and a  $WTi_x$  solid solution is formed, thereby improving the ductility and retaining the integrity of the projectile under explosions, even during propellant loading [15].

Other factors influence the reactivity during dynamic deformation. For example, Luo et al. proposed that higher free energy caused by the irregular arrangement of atoms is why W-Zr-based metallic glass composites are more reactive than W-Zr alloy composites [13]. Through mesoscale simulations, Aydelotte et al. suggested that the topology of the microstructure constituents in binary powder mixtures, particularly the stronger phase, plays a significant role in regulating impact-induced reactions [16]. Materials in which the hard phase is topologically connected are more likely to react at a lower impact velocity due to plastic deformation at higher temperatures. Moreover, Wang et al. found that in TiZrNbTa high-entropy alloys, the dislocation pipe effect, caused by more severe lattice distortion and more dislocations, leads to a higher diffusion rate of oxygen atoms and higher oxidation rate [17]. This finding showed that HEAs composed of highly-exothermic elements are expected to have a higher energy release rate and release abundant energy when they react with atmospheric oxygen.

Therefore, HEAs have attracted widespread attention in the field of ESMs due to their unique structure, intrinsic severe lattice distortion, and excellent mechanical properties [18–20]. Different from the traditional alloy-design concept, HEAs contain multiple principal elements, often five or more in an equal or near-equal atomic percentage (at.%) [21,22]. There are number of possible compositions and combinations of properties in the HEA field. Therefore, it is possible to tailor the material properties to meet the requirements for ESMs with high strength and high energy density [23,24]. For instance, Zhang et al. designed a HfZrTiTa<sub>0.53</sub> HEA with a dual-phase BCC structure and found that it displays thermoplastic instability [9]. Highly-localized adiabatic shear deformation in the ductile phase plays a vital role in the failure mechanism under a dynamic load, demonstrating a prominent strain-rate strengthening effect, while the ductility is not compromised and remained at roughly 9%–13% [9]. However, excessively high plastic deformation (>10%) diminishes its ability to form smaller fragments, which is detrimental to the release of chemical energy after impact deformation [9]. Thus, it is important to design a new type of ESMs with a combination of high strength, appropriate plasticity, high density, and good energetic characteristics. This requires understanding the relationship between the microscopic deformation mechanism and the energy release mechanism.

In this study, a novel hierarchical triple-phase TiZrHfTa<sub>0.7</sub>W<sub>0.3</sub> HEA was fabricated by vacuum electromagnetic levitation melting. In addition to the main metastable BCC (denoted as BCC1) matrix, the hierarchical microstructure was composed of different morphologies and size scales, including Ta-W-rich BCC (denoted as BCC2) precipitates and interwoven HCP lamellar nanoplates em-

bedded in the BCC1 matrix. The metastable BCC1 phase transformed into the HCP phase during deformation and displayed transformation-induced plasticity (TRIP), which provided enhanced strength and plasticity at a high strain rate to maintain the integrity of the projectile. Moreover, it possessed greater transverse destructive characteristics compared with commonly used materials such as tungsten heavy alloys during penetration tests. The significant mechanical properties and destructive characteristics demonstrate its potential as a desirable ESM.

## 2. Experimental

The TiZrHfTa<sub>0.7</sub>W<sub>0.3</sub> refractory HEA was prepared with electromagnetic levitation melting in a water-cooled copper crucible under a 0.08 Pa argon atmosphere. The vacuum electromagnetic levitation melting method remains the metallic materials in levitation during the melting process, avoiding the contact between the melted materials and the crucible to prevent potential contamination. Meanwhile, the strong electromagnetic stirring during the melting process also ensures a uniformity of temperature and chemical composition inside the sample [25]. Electromagnetic levitation melting was first used to prepare a W-Ta master alloy that was remelted five times. Then, the master alloy was melted with Hf, Zr, and Ti elements successively and then remelted three times. To fully dissolve these five elements, each melting time was about 20 min. After cooling, the bulk ingot was shaped into dimensions of approximately 60 mm in length and 80 mm in diameter, with a density of about 10.1 g/cm<sup>3</sup>.

The crystal structures of the bulk alloy were analyzed by X-ray diffractometry (XRD, RIGAKU-D Smartlab 9 kW) with  $Cu-K\alpha$  radiation scanning from 20° to 120° at a scanning rate of 2°/min. Electron backscattered diffraction (EBSD) was conducted using a field emission scanning electron microscope (SEM, JSM-7100F) equipped with an EDAX-TSL OIM EBSD system. The EBSD samples were prepared by mechanical grinding using 1200 to 3000 grit SiC papers followed by a final polishing step using a 20 nm alumina oxide particle suspension (OPS). The chemical composition analysis was conducted by energy-dispersive X-ray spectroscopy (EDS) on a Schottky field emission scanning electron microscope (FE-SEM, Hitachi SU5000). The microstructures of the as-cast samples were further characterized by transmission electron microscopy (TEM, JEM-2100F at 200 kV). A focused ion beam (FIB) instrument (FEI Scios 2 DualBeam) was used to prepare TEM samples from the as-cast sample. The oxidation state on the fracture surface of deformed samples was analyzed by X-ray photoelectron spectroscopy (XPS, Thermo ESCALAB 250Xi) and EDS line scans by SEM (Zeiss Supra 35VP). In addition, differential scanning calorimetry (DSC, Netzsch 404) was also employed to assess the reactivity of the TiZrHfTa<sub>0.7</sub>W<sub>0.3</sub> HEA under the argon and air atmosphere. The heating rate was 20 °C/min.

Cylindrical samples with dimensions of  $\Phi 4$  mm  $\times$  8 mm and  $\Phi 4$  mm  $\times$  4 mm were prepared to perform the quasi-static and dynamic uniaxial compression tests, respectively. The quasi-static tests were conducted at a strain rate of  $5 \times 10^{-4}$  s<sup>-1</sup> with a CMT5105S material test system at ambient temperature. Dynamic compression tests were performed on a split Hopkinson pressure bar (SHPB) apparatus. In the SHPB experiments, the different strain rates were controlled by the impact velocity. The compression tests for each strain rate were repeated at least 3 times.

Penetration tests were performed using a 30 mm smooth-bore ballistic range (DBR30) driven by gaseous detonation, which was designed and built by the Institute of Mechanics, Chinese Academy of Sciences. The device and experimental layout are shown in Fig. 1. Conventional maraging stainless steel (18Ni (350), 7.9 g/cm<sup>3</sup>) and WC alloy (YL10.2, 14.5 g/cm<sup>3</sup>) specimens were also tested as the ballistic projectiles for comparison. All TiZrHfTa<sub>0.7</sub>W<sub>0.3</sub>, 18Ni

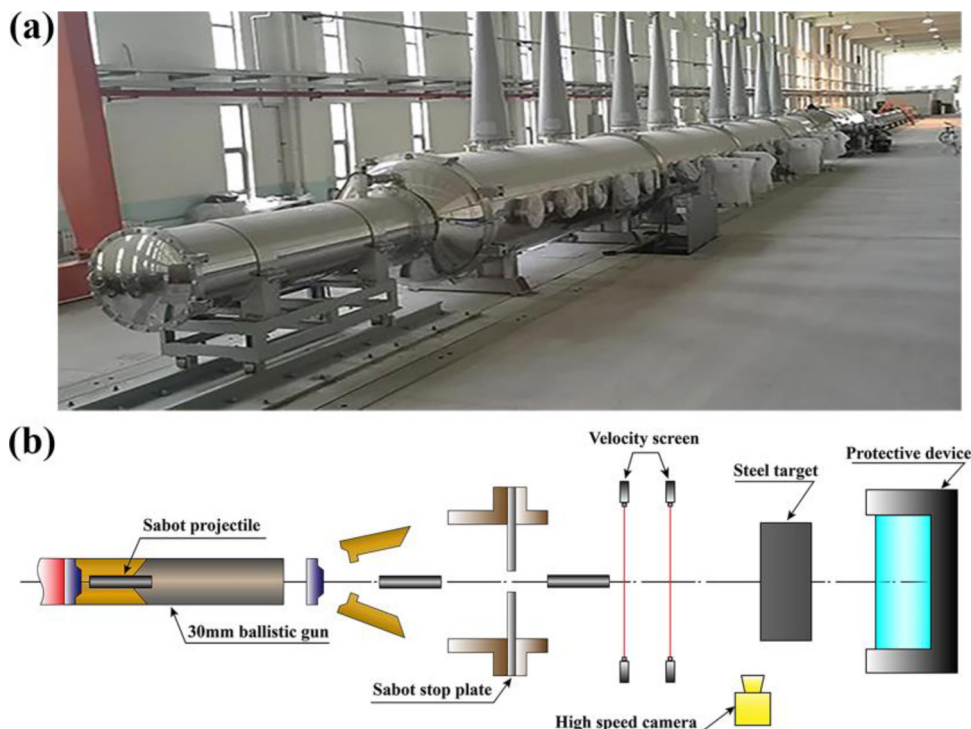


Fig. 1. (a) Gaseous-detonation driven ballistic range DBR30 device and (b) experimental layout for the penetration tests.

(350), and YL10.2 projectiles were machined into rods with dimensions of  $\Phi 8 \text{ mm} \times 40 \text{ mm}$ . To fire a smaller rod by the smooth-bore with a larger diameter, a sabot was employed, which consisted of two separate parts and a bottom pusher. The penetration experiments were conducted in a sealed testing chamber under an atmospheric condition with a pressure of 10 kPa. The medium-carbon steel target 100 mm in thickness (which can be considered as a semi-infinite target) was placed 5 m in front of the ballistic range. A laser velocimetry system was utilized to measure the impact velocity, and it was positioned 2 m in front of the target. The measured velocities for TiZrHfTa<sub>0.7</sub>W<sub>0.3</sub>, 18Ni (350) and YL10.2 specimens are  $2.053 \pm 0.010$ ,  $2.248 \pm 0.015$  and  $2.248 \pm 0.015$  km/s, respectively. The penetration processes were recorded by a high-speed camera. After ballistic tests, the targets with craters were sectioned along the plane of symmetry by wire electrical discharge machining to evaluate the penetration performance. The penetration tests for each type of projectile were repeated 2 times.

### 3. Results and discussion

#### 3.1. Microstructural characterization

Fig. 2 shows a typical analysis of the microstructure of the as-cast TiZrHfTa<sub>0.7</sub>W<sub>0.3</sub> HEA. Diffraction peaks corresponding to a body-centered cubic (BCC) and a hexagonal close-packed (HCP) structure are observed in the XRD pattern in Fig. 2(a). Fig. 2(b-d) shows the corresponding average grain size  $\bar{d}$  in Fig. 2(c), the EBSD inverse pole figure (IPF) map, and phase map, respectively. The average grain size  $\bar{d}$  is approximately 117  $\mu\text{m}$ , which is similar to other as-cast refractory high-entropy alloys with coarse crystal characteristics [26–29]. The IPF map shows no preferential orientation of the BCC phases in the as-cast sample, indicating that the sample is homogeneous. The EBSD phase images only show a BCC structure, but there may be a nanoscale HCP phase embedded in the matrix according to the XRD pattern [30]. Fig. 3 shows the

backscattered electron (BSE) image and the element distributions near the grain boundary. Many dendrites are distributed within the coarse grains and massive nanoprecipitates are distributed at the grain boundary and dendritic intervals, representing a multi-phase hierarchical microstructure [31]. Moreover, the SEM-EDS results show that Ti and Hf atoms tended to segregate in the grain, while Ta and W tend to segregate at the grain boundary, and Zr is evenly distributed in the alloys.

To verify the precipitates' structure and HCP nanophases suggested in the XRD data (Fig. 2(a)), selected area electron diffraction (SAED) patterns and TEM-EDS were used, and the results are shown in Fig. 4. Fig. 4(a) shows the selected area of the FIB samples near the grain boundaries, including the matrix, precipitates, and their SAED patterns, respectively. The bright-field TEM image shows the size of clustered round-shape precipitates is less than 1  $\mu\text{m}$ , even down to about 10–20 nm. Through the SAED patterns and the high-angle annular dark-field (HAADF) images in Fig. 4(b), in addition to the main metastable BCC1 matrix, interwoven HCP lamellar nanoplates are embedded in the BCC1 matrix, and other Ta-W-rich BCC2 precipitates are diffusely distributed in it. Furthermore, the two BCC phases have similar lattice parameters of 3.296  $\text{\AA}$  and 3.202  $\text{\AA}$  for the BCC1 matrix and BCC2 precipitates, respectively. The lattice parameters of the HCP phase are  $a = 3.079 \text{ \AA}$  and  $c = 5.018 \text{ \AA}$ .

To determine the distribution of constituent elements, the TEM-EDS maps of the red rectangular region in Fig. 4(a) were measured, as shown in Fig. 4(b). It is seen that Ta and W segregate in the BCC2 precipitates which may induce nanoprecipitates strengthening [32], while Ti, Zr, and Hf are rich in the matrix. There is only a small difference in the elemental composition of BCC and HCP in the matrix, and the Hf content in the HCP phase is slightly higher than that in the BCC1 phase. The fast Fourier transformation along [210] and [10 $\bar{1}$ 1] zone axes further confirms the presence of an HCP phase structure in the BCC1 matrix, although they are barely distinguishable in Fig. 4(b). In addition, the BCC1 matrix of TiZrHfTa<sub>x</sub> is metastable and further destabilizes as the Ta content

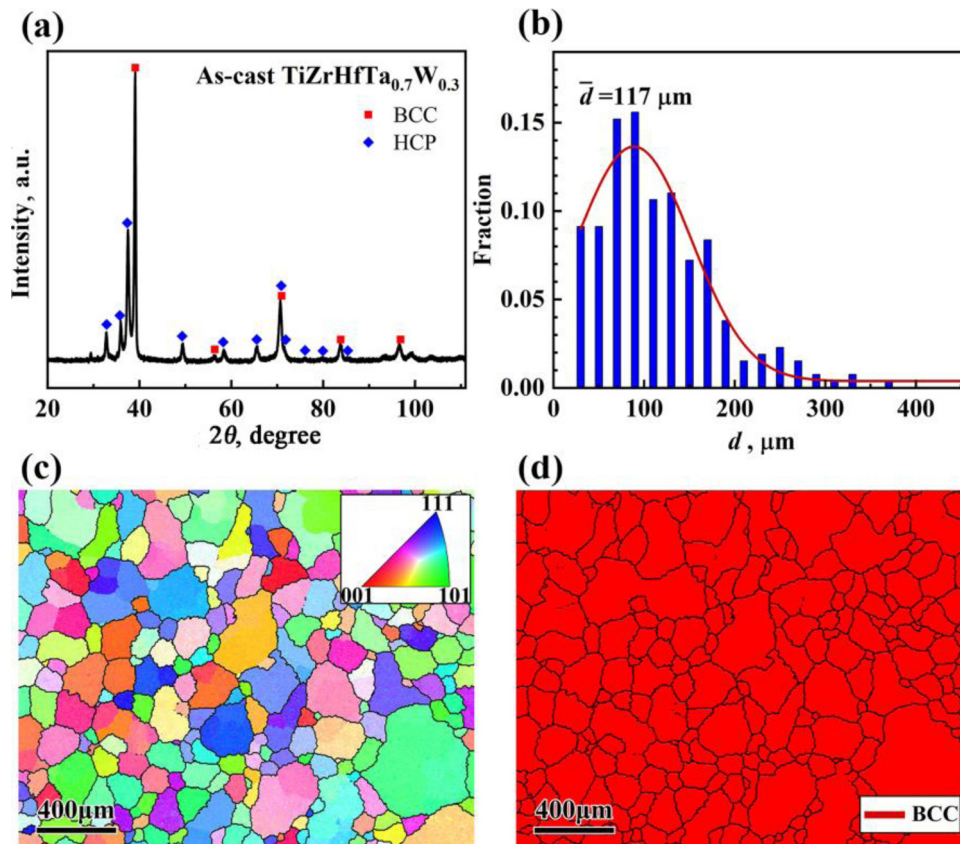


Fig. 2. (a) XRD pattern of the as-cast TiZrHfTa<sub>0.7</sub>W<sub>0.3</sub> sample, (b) grain size distribution with the region in (c), (c) EBSD IPF map, (d) phase map.

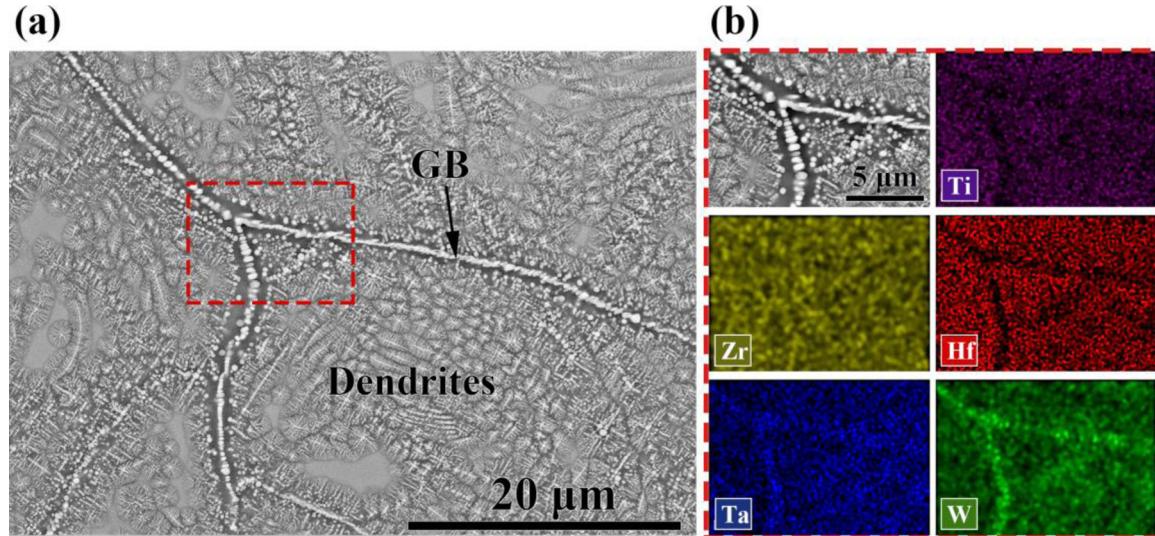


Fig. 3. (a) BSE image near the grain boundary and (b) SEM-EDS element distribution of the red dashed region in (a).

decreases [30,33,34]: when  $x < 0.6$ , it can produce a dual-phase microstructure consisting of HCP lamella embedded in a BCC matrix. The potency of the transformation from BCC to HCP decreases after increasing Ta content during deformation [30]. Therefore, the BCC1 phase with similar constituents in this work may also be a metastable phase, indicating that the transformation from BCC1 to HCP can be easily initiated during deformation. Based on all the results above, BCC2 precipitates will be formed with the addition of W element, which helps decrease Ta content in the BCC1 matrix and form an HCP phase; meanwhile, the BCC1 matrix is destabilized.

### 3.2. Dynamic mechanical properties

The engineering stress-strain curves of the TiZrHfTa<sub>0.7</sub>W<sub>0.3</sub> HEA tested at room temperature for various strain rates ( $10^{-4}$  s<sup>-1</sup>–4200 s<sup>-1</sup>) are displayed in Fig. 5(a). Compared with quasi-static ones, the dynamic yield strength is dramatically increased from 1500 to 1940 MPa when the strain rate rises to 4200 s<sup>-1</sup>. Moreover, the ultimate strength is also enhanced with the increasing strain rate. A previous study showed that the yield strength in BCC metals is mainly controlled by the dislocation thermal activation mechanism [35]. The thermal energy can decrease the height

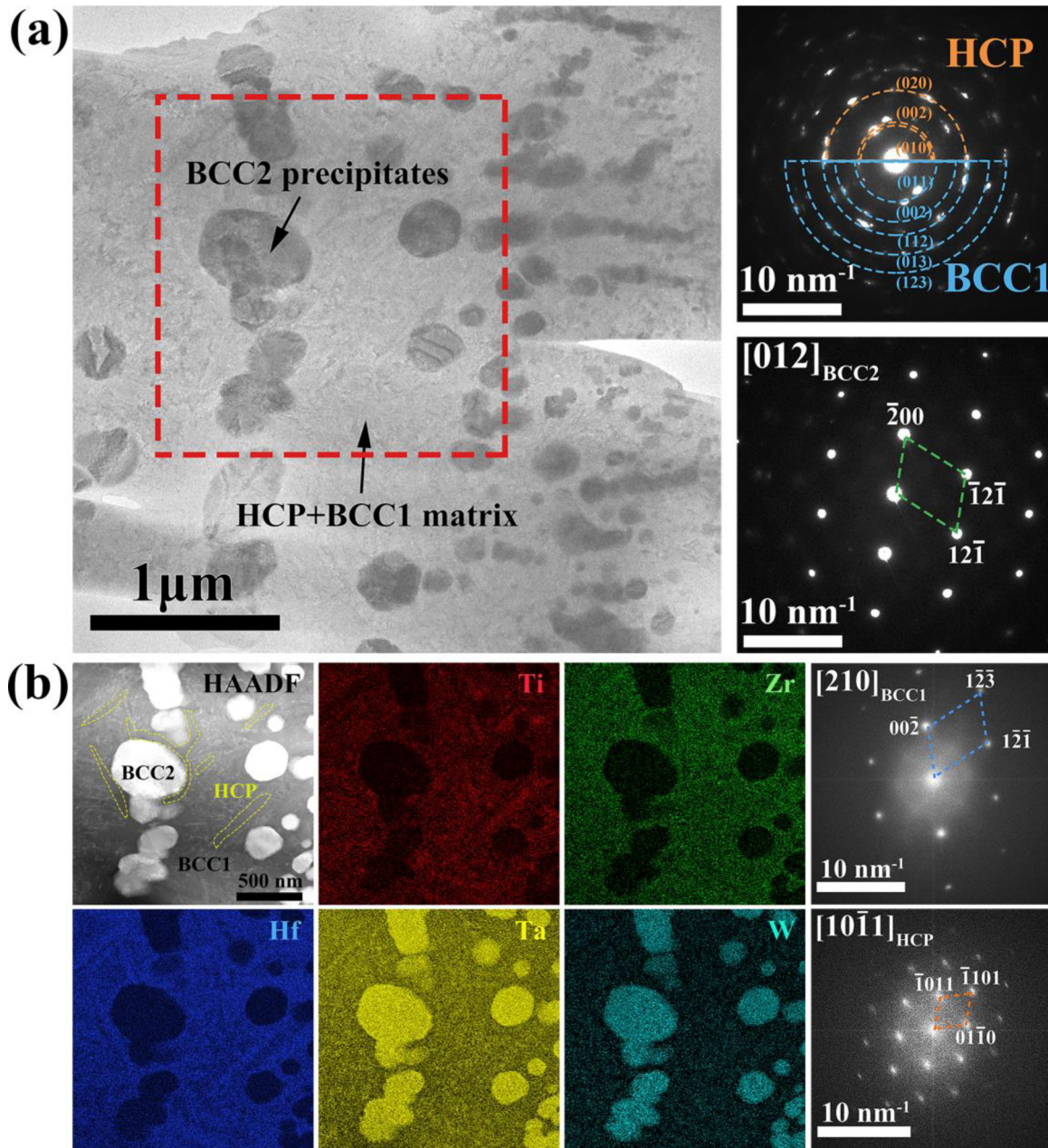


Fig. 4. (a) Selected area of the FIB-TEM sample and corresponding SAED patterns of the precipitates and the matrix; (b) TEM-EDS maps of the red region in (a) and the corresponding fast Fourier transform patterns of the BCC1 and HCP matrix.

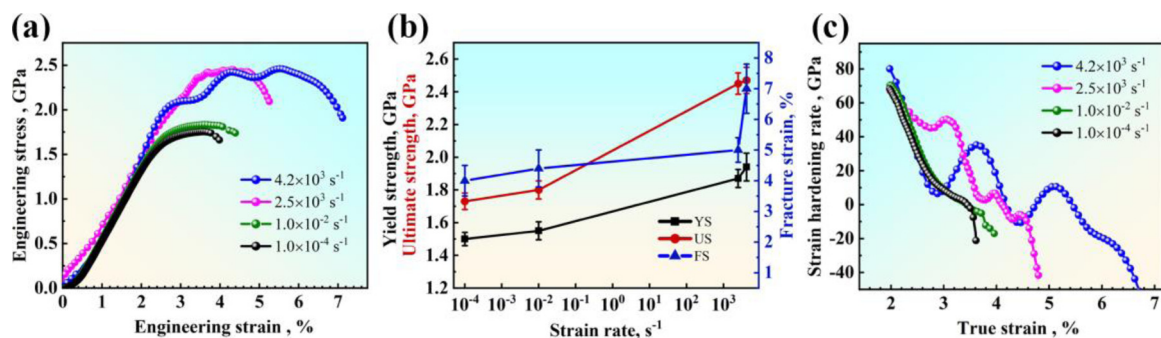


Fig. 5. Compressive mechanical properties at various strain rates of the TiZrHfTa<sub>0.7</sub>W<sub>0.3</sub> HEA: (a) engineering stress-strain compression curves; (b) yield strength (YS), ultimate strength (US), and fracture strain (FS); (c) corresponding strain hardening rates.

of the short-range barrier, which is beneficial for dislocations to overcome these obstacles [36]. However, with an increasing strain rate, there is less time available for dislocations to cross the barrier and the thermal energy will be less effective [35]. Thus, the TiZrHfTa<sub>0.7</sub>W<sub>0.3</sub> HEA in this study possesses higher strength under dynamic loading, and there is a positive correlation between the yield strength and the strain rate.

Surprisingly, opposite to the other HEAs [37,38], the dynamic plasticity is not compromised during dynamic deformation. The fracture strain increases from 4.0% to 7.0% (Fig. 5(b)), and this HEA still possesses good plastic flow behavior with significant stress fluctuations. Generally, the plasticity would be sacrificed as the strain rate increases which is mainly due to the adiabatic softening effect [35]. In the present study, the enhancement of plasticity may attribute to the phase transformation from BCC1 to HCP phase. As shown in Fig. 4, the metastable BCC1 phase is prone to transform into HCP phase during deformation, especially in the dynamic regime with a high-temperature rise [39]. The phase transformation can introduce a significant strain-hardening effect (Fig. 5(c)) by dynamic strain/stress partitioning between BCC1 and HCP phases, which subsequently promotes a continuous plastic deformation in BCC1 matrix [24]. In addition, the phase transformation can also release the stress concentration on the interface between these two phases. Thus, both the ultimate strength and plasticity were significantly enhanced due to the transformation hardening and interface hardening from such metastable transition [30].

Besides, the fluctuations in the stress-strain curve at high strain rates were mainly due to the competition between thermal softening and work hardening [40]. Under impact loading, the localized plastic deformation tends to occur with a temperature rise. The temperature rise can cause significant thermal softening for this HEA with low intrinsic specific heat capacity and thermal conductivity [41], giving a considerable fluctuation in the plastic flow at the strain rate of 4200 s<sup>-1</sup>. Moreover, this temperature rise can also induce the formation of adiabatic shear deformation, contributing to the energy release characteristics which may play a significant role in improving penetration performance.

### 3.3. Microstructural evolution and energetic characteristics

In order to better understand the dynamic deformation and the energy release process, a high-speed camera was used to capture the SHPB compression test processes. Fig. 6 shows the compression test under a strain rate of 4200 s<sup>-1</sup>. Initially, the specimen undergoes a conventional compression deformation that compressive strain accumulates with the impact of the Hopkinson bar until 6.0% around 40 μs. As the impact of the Hopkinson bar continues, at around 50 μs, the fracture surface appears with a 45° shear angle. However, different from the conventional failure of metallic material, incandescent light is observed along the fracture surface in the investigated HEA, showing a significant energy release characteristic, which subsequently becomes more intense as the loading continues. From DSC results as shown in Fig. S1 in Supplementary Information, this energy release behavior can mainly be attributed to the oxidation with atmospheric oxygen [9].

Moreover, the fracture surface of the sample remnants was investigated by SEM, and the corresponding EDS line profiles are shown in Fig. 7. In Fig. 7(a), the fracture surface shows a river-like pattern but with small dimples, indicating that the failure mode is a mainly brittle fracture, with little plasticity. There are many molten particles (MPs) smaller than 100 μm attached to the fracture surface due to the high temperature produced by the oxidation of active elements. The fracture morphology of the matrix in the enlarged yellow region also shows the melting characteristics. In addition, the corresponding EDS line profiles of regions

b and c are shown in Fig. 7(b) and (c), respectively. The fluctuations in the concentration of oxygen elements show that the MPs are mostly oxides, and the matrix is also slightly oxidized. It can be inferred that almost all fracture surfaces undergo oxidation. Because the temperature rise at the tip of the crack is very high, the “hot spots”, where the reaction is initiated, can be easily formed at the fracture surface [42]. In addition, there are many sub-nano/nanosized BCC2 nanoprecipitates that improved the hard phase topological connectivity of the structure, which promoted the reaction by reducing its activation energy [16]. Irregular MPs similar to the composition of the matrix are located in region b, and Zr-rich spherical particles smaller than 1 μm are observed in region c. These irregular MPs are numerous and larger, which are the oxidation products of fragments inside the grain, as indicated by Fig. 7(b) and (c). The Zr-rich oxide particles may be produced by oxidation near grain boundaries because Zr atoms are more uniformly distributed in the matrix than Ti and Hf, which are relatively sparse at grain boundaries, as shown in Fig. 4(b). Therefore, it can be inferred that the nano-/microscale particles will be easily produced at the fracture surface which will also facilitate the reaction.

To investigate the oxidation states of the constituent elements on the fracture surface, XPS analysis was performed to further study the energetic characteristics of the investigated HEA. As shown in Fig. 8, oxide peaks appear for Ti, Zr, Hf, Ta, and W elements, which indicates that these elements were all involved in the oxidation reaction. Hf, Ta, and Zr are the most sufficiently oxidized. Their oxidation products are HfO<sub>2</sub>, Ta<sub>2</sub>O<sub>5</sub>, and ZrO<sub>2</sub>, whose percentages are 96%, 92%, and 87%, respectively. Ti and W are relatively inert, since their oxidation percentages are 60% and 64%, respectively. The refractory elements in this HEA have a high affinity for oxygen at high temperatures, but the dense protective oxidate film of TiO<sub>2</sub> prevents the oxygen element from diffusing, and so, only 60% Ti element is oxidized [43]. On the contrary, due to the lack of protective oxidate film, Hf, Ta and Zr elements are oxidized more sufficiently. It is worth noting the function of WO<sub>3</sub> that it cannot only allow oxygen to permeate and diffuse [44], but can also sublime very quickly with a temperature higher than 900 °C leaving a “porous” structure to further promote the oxidation by providing more contact area with oxygen [45]. This can reduce the oxidation resistance of the oxide scale and make the alloy more susceptible to oxidation to release more energy. Moreover, WO<sub>3</sub> can also react with Ta element to further facilitate the redox reaction [46]. The oxygen atom can diffuse easily and oxidize with the Ta-W-rich BCC2 precipitates during the combustion reaction. Thus, when subjected to high-strain-rate loads, the TiZrHfTa<sub>0.7</sub>W<sub>0.3</sub> HEA is susceptible to violent energy release reactions.

### 3.4. Hypervelocity penetration and ballistic characteristics

To explore the potential of this HEA as an ESM, the penetration performance of this HEA under high-velocity impact was investigated through ballistic penetration experiments. And the penetration process was captured by a high-speed camera. During the penetration, the HEA goes through combustion giving out energy as well as incandescent light. The generation of incandescent light can obscure the observation of the penetration process. So, optical filters were applied together with a background light source to get a clear view of the penetration in our study as shown in Fig. 9(a). However, the penetration was also filmed without filters as shown in Fig. 9(b) exhibiting a more violent energy release behavior compared to other conventional structural materials [47].

To further investigate the penetration performance, we investigated the cross-sectional morphology of the target plates. Generally, the penetration performance is characterized by the depth

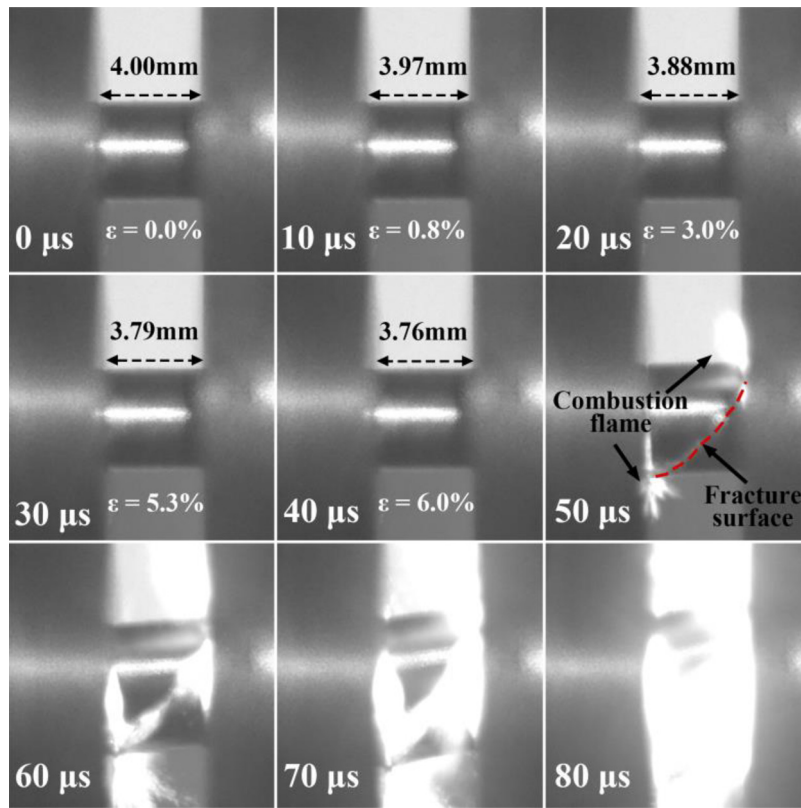


Fig. 6. High-speed photographs during Hopkinson bar impact tests ( $\dot{\epsilon} = 4200 \text{ s}^{-1}$ ), where the sample failed at 50  $\mu\text{s}$ , and metal combustion was observed along the fractured surface.

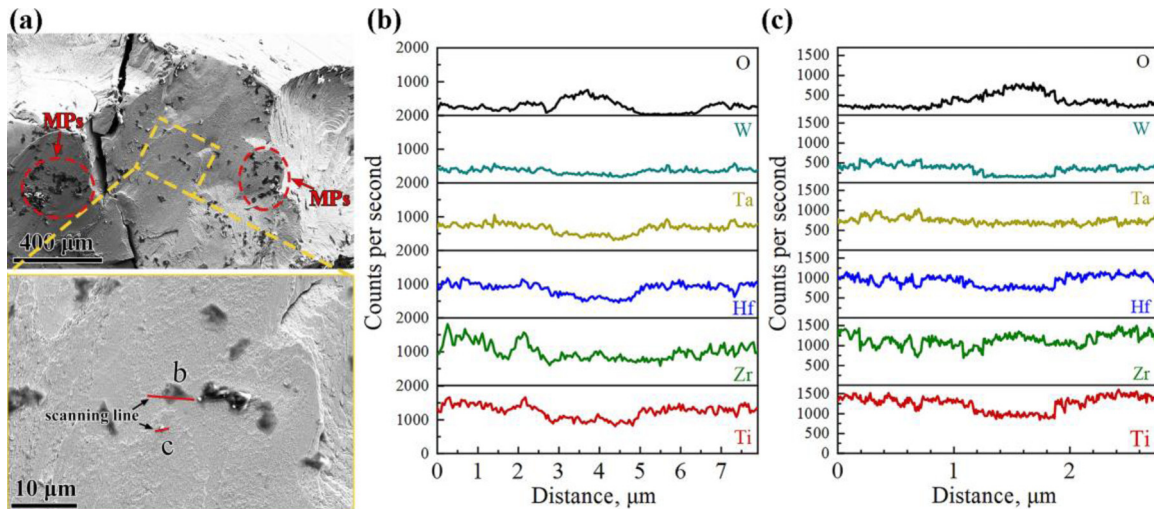


Fig. 7. (a) Remnant fracture surface at  $4200 \text{ s}^{-1}$ . Red circles mark a large number of molten particles, and the two red lines (denoted as b and c) in the yellow region are for the EDS line scanning; (b, c) corresponding EDS line profiles for lines b and c in (a), respectively.

and diameter of the penetration channel, which represent longitudinal damage and transverse damage, respectively [48–53]. Assuming that the cross-section of the penetration channel along the depth direction is circular, the volume of the penetration channel  $V_p$  can be estimated by Eq. (1):

$$V_p = \int_0^P \frac{\pi D(h)^2}{4} dh \approx \sum \frac{\pi D(h)^2}{4} \Delta h \quad (1)$$

where  $P$  is the penetration channel depth,  $D(h)$  is the penetration channel diameter as a function of the penetration channel depth, and  $\Delta h$  is the integration step, here,  $\Delta h = 1 \text{ mm}$ . Fig. 10(a)

shows the cross-sections of the steel target plate with the WC (YL10.2) alloy, TiZrHfTa<sub>0.7</sub>W<sub>0.3</sub> HEA, and 18Ni stainless steel cylindrical projectiles. The average value and relative error of penetration channel depths of the YL10.2 alloy and 18Ni stainless steel projectiles are  $49.0 \pm 1.5$  and  $35.0 \pm 0.8$  mm, respectively; the maximum penetration channel diameters for them are  $19.1 \pm 0.2$  and  $20.9 \pm 0.2$  mm, respectively. Nevertheless, the HEA projectile exhibits a medium penetration depth and maximum penetration channel diameter of  $43.5 \pm 1.0$  and  $23.0 \pm 0.1$  mm. The maximum diameter of the HEA investigated in this study is, therefore, larger than those of YL10.2 and 18Ni by 20.42% and 10.05%, respectively,

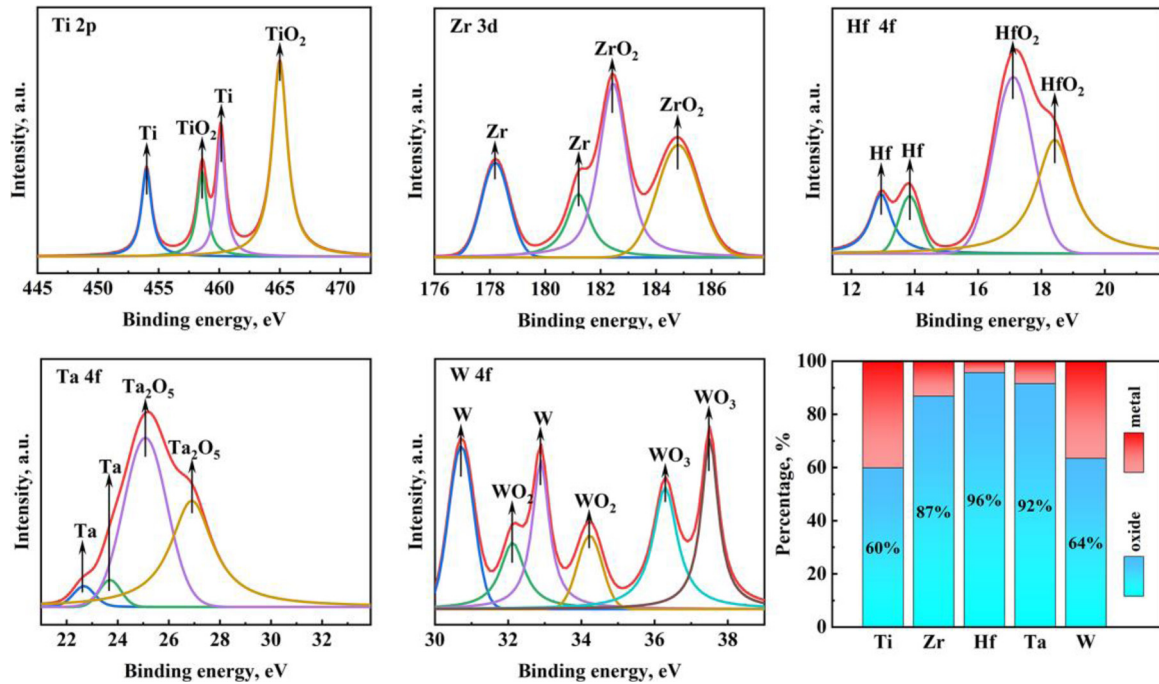


Fig. 8. XPS spectra of Ti, Zr, Hf, Ta, and W elements on the fracture surface at 4200 s<sup>-1</sup> and the percentage of metals and metal oxides.

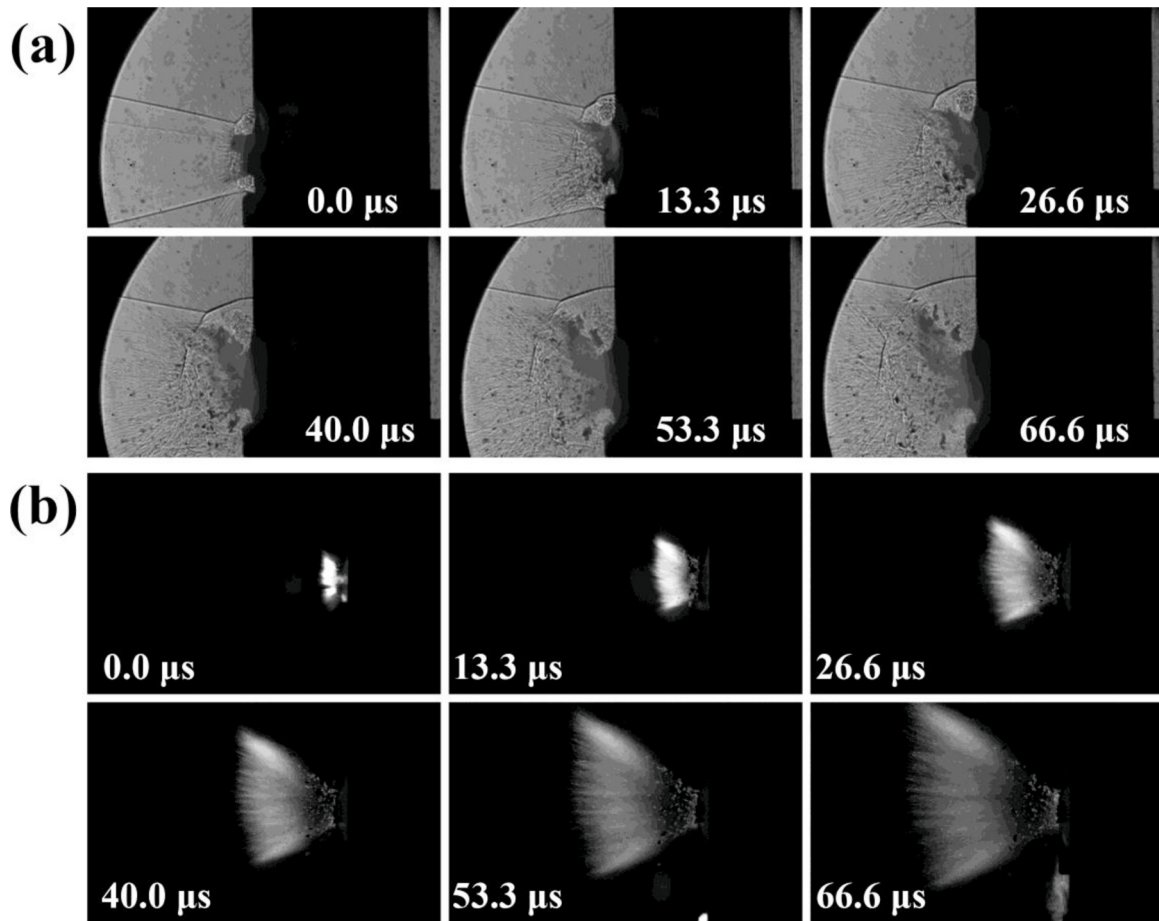
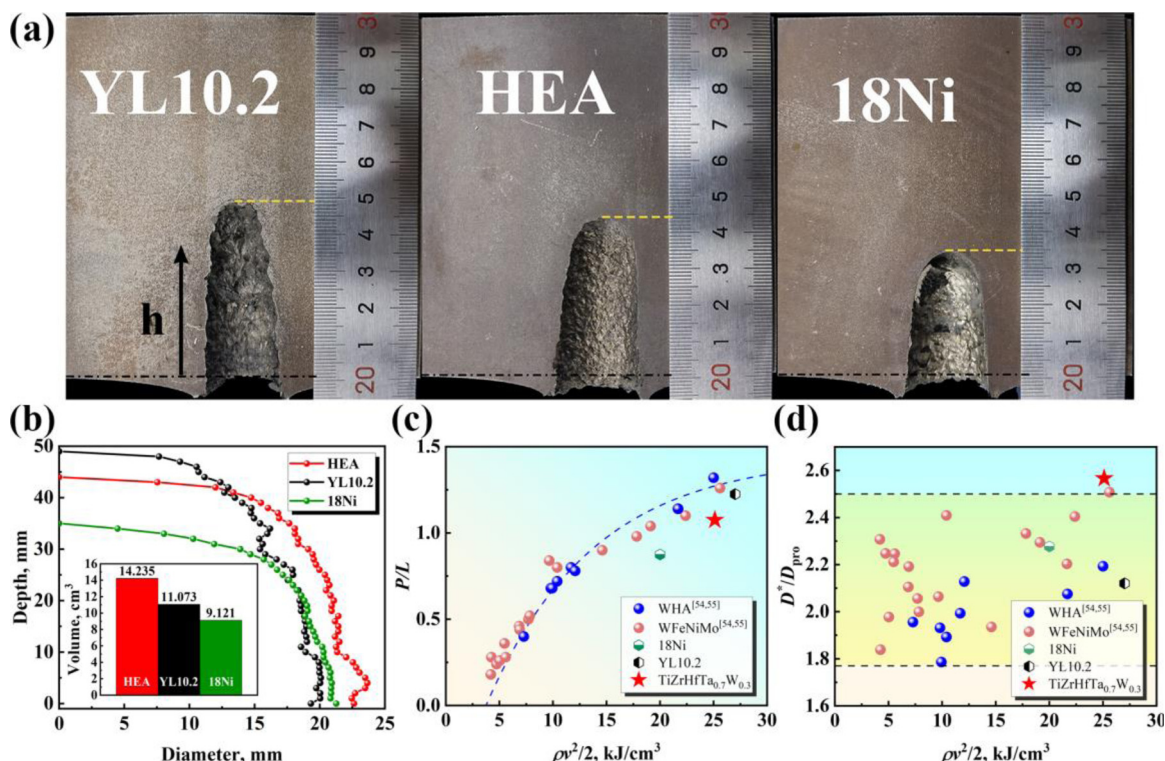


Fig. 9. High-speed video frames of the penetration process of TiZrHfTa<sub>0.7</sub>W<sub>0.3</sub> HEA projectiles: (a) with optical filters and background light source, (b) without optical filters and background light source.



**Fig. 10.** (a) Cross-section of the target plate with YL10.2 alloys (left), HEA in this study (middle), and 18Ni stainless steel (right) cylindrical projectiles; (b) hole diameter vs. depth diagram, and the inset is the volume of penetration channel; (c) relationship of kinetic energy with  $P/L$ ; (d) relationship of kinetic energy with  $D^*/D_{pro}$ .

showing a better hole-enlarging capability, which is also demonstrated by the proposed dimensionless equivalent diameter as follows.

Moreover, the volume of the penetration channel is  $14.235 \text{ cm}^3$ , showing the superior expansion of the HEA, as shown in Fig. 10(b). Although the final penetration depth is lower than the LY10.2, the penetration channel volume of the HEA is 28.6% higher than that of the LY10.2 under high kinetic energy (near  $25 \text{ kJ/cm}^3$ ). In addition, assuming that the penetration channel is cylindrical with an equivalent diameter  $D^* = 2\sqrt{V_p/(P\pi)}$  and the same final penetration depth, the longitudinal and transverse destruction characteristics can be expressed in terms of the dimensionless penetration depth  $P/L$  ( $L$  is the length of the projectile) and the dimensionless equivalent diameter  $D^*/D_{pro}$  ( $D_{pro}$  is the diameter of the projectile).

The relationships of  $P/L$  and  $D^*/D_{pro}$  with different projectiles and kinetic energies are shown in Fig. 10(c) and (d), respectively. The  $P/L$  of TiZrHfTa<sub>0.7</sub>W<sub>0.3</sub> HEA and LY10.2 are slightly lower than those of WHA (tungsten heavy alloy,  $17.5 \text{ g/cm}^3$ ) and WFeNiMo HEA ( $12.5 \text{ g/cm}^3$ ) under high kinetic energy of  $25 \text{ kJ/cm}^3$  [54,55]. Under the impact velocity near  $2 \text{ km/s}$ , the materials behave like a liquid, and the dominant physical property in this scenario is the density of the material. And, therefore, in this study, the strength of the projectiles and target plates are not considered. According to the jet penetration theory [56], the penetration depth can be simply expressed as:

$$P/L = \sqrt{\frac{\rho_{pro}}{\rho_t}} \quad (2)$$

where  $\rho_{pro}$  and  $\rho_t$  are the density of the projectile and target, respectively. The  $P/L$  value was positively correlated with the density of the projectile for the same target material. Therefore, the projectile density is the main reason that the longitudinal destruction ability of the TiZrHfTa<sub>0.7</sub>W<sub>0.3</sub> HEA was lower than other high-density materials.

The dimensionless equivalent diameter  $D^*/D_{pro}$  shows the superior transverse destruction ability of the TiZrHfTa<sub>0.7</sub>W<sub>0.3</sub> HEA due to its high energy characteristics and lower reaction threshold. During the normal penetration process, since the longitudinal pressure is much higher than the transverse pressure, the overpressure generated by the deflagration of energetic materials hardly enhances the longitudinal damage capacity, while the transverse damage capacity can be significantly enhanced. The dimensionless equivalent diameter  $D^*/D_{pro}$  of the TiZrHfTa<sub>0.7</sub>W<sub>0.3</sub> HEA is  $2.53 \pm 0.03$ , whereas  $D^*/D_{pro}$  for YL10.2 and 18Ni is  $2.12 \pm 0.03$  and  $2.28 \pm 0.02$ ; the hole-enlarging capability of TiZrHfTa<sub>0.7</sub>W<sub>0.3</sub>, therefore, increases by 19.3% and 11.0%. In addition, this hole-enlarging capability is also higher than those of WHA and WFeNiMo HEA in literature [54,55]. The heats of reaction of the combustion of some commonly-used metals to metal oxide are listed in Table S1 in Supplementary Information. The theoretical heat of reaction of TiZrHfTa<sub>0.7</sub>W<sub>0.3</sub> is  $7.93 \text{ kJ/g}$  or  $80.09 \text{ kJ/cm}^3$ , which is a high value considering the trade-off between mechanical properties and the heat of reaction. Although the theoretical heat of reaction of WFeNiMo is  $5.75 \text{ kJ/g}$  or  $75.39 \text{ kJ/cm}^3$ , the reactivity of the alloy constituents affects the actual combustion reaction. The presence of Ta-W-riched nanoprecipitates plays an important role in the oxidation reaction, where  $\text{WO}_3$  can not only catalyze Ta reaction, but also sublimate at high temperatures to form voids on the surface of the alloy. In our experiments, there were nearly no large remnants of TiZrHfTa<sub>0.7</sub>W<sub>0.3</sub> projectile in the penetration channel, in contrast to those of 18Ni and YL10.2 projectiles, which still have some remnants in the crater. This indicates that the kinetic and chemical energy has been more sufficiently converted into the energy which is needed for penetrating the crater. This is also the reason why the TiZrHfTa<sub>0.7</sub>W<sub>0.3</sub> HEA shows a higher penetration channel volume with the comparable kinetic energy [56]. Therefore, the TiZrHfTa<sub>0.7</sub>W<sub>0.3</sub> HEA shows a superior hole-enlarging capability and is a great candidate material for defense and military applications.

#### 4. Conclusions

In this work, a hierarchical triple-phase metastable TiZrHfTa<sub>0.7</sub>W<sub>0.3</sub> high-entropy alloy with high energy release characteristics was fabricated. It was subjected to a series of experiments under quasi-static and dynamic load to characterize its energy release capability and mechanical properties to assess its potential structural applications. Its mechanical properties were then investigated in terms of microstructural evolution, which was then related to the strain rate. The energy release was investigated in terms of the chemical composition of the combustion products. Finally, this HEA was tested by high-velocity penetration to demonstrate its potential engineering applications. The major conclusions are:

- (1) This HEA consisted of three distinct phases, the Hf-Zr-rich HCP, BCC1 matrix, and Ta-W-rich BCC precipitates. Under quasi-static loading, precipitation hardening was the dominant strengthening mechanism. Hf-Zr-rich HCP lamellae nanoplates and Ta-W-rich BCC nanoprecipitates co-contributed to the high strength by hindering dislocation movement.
- (2) This HEA showed a prominent strain rate strengthening effect when the strain rate increased from  $1.0 \times 10^{-4} \text{ s}^{-1}$  to  $4.2 \times 10^3 \text{ s}^{-1}$ , while the plasticity was not compromised and the fracture strain remained in the range of 4.0%–7.0%. This was mainly attributed to the TRIP effect caused by the transformation of the BCC1 phase to the HCP phase.
- (3) According to the EDS line profiles and XPS analysis, the W element complicated the microstructures by forming precipitates and promoting the segregation of Ta in the matrix. It also promoted the oxidation of Ta, resulting in a higher energy release effect and a lower threshold for the combustion reaction.
- (4) TiZrHfTa<sub>0.7</sub>W<sub>0.3</sub> exhibited significant chemical energy release and high energy release capacity during high-velocity penetration, leading to excellent hole-enlarging efficiency. The combination of excellent mechanical properties and energetic characteristics demonstrates its great potential as a novel high-strength ESM.

#### Acknowledgments

This work was financially supported by the National Natural Science Foundation of China (Nos. 51401028, 51271193 and 11790292), the Strategic Priority Research Program of the Chinese Academy of Sciences (No. XDB22040303), and the Innovation Program (No. 237099000000170004).

#### References

- [1] R. Ames, MRS Online Proceedings Library (OPL) 896 (2005). doi:10.1557/PROC-0896-H03-08.
- [2] M. Wang, J. Li, J. Zhang, X. Liu, Z. Mao, Z. Weng, H. Wang, J. Tao, J. Mater. Eng. Perform. 29 (2020) 506–514.
- [3] X.F. Zhang, A.S. Shi, L. Qiao, J. Zhang, Y.G. Zhang, Z.W. Guan, J. Appl. Phys. 113 (2013) 083508.
- [4] Q. Zhou, Q. Hu, B. Wang, B. Zhou, P. Chen, R. Liu, J. Alloy. Compd. 832 (2020) 154894.
- [5] D.L. Hastings, E.L. Dreizin, Adv. Eng. Mater. 20 (2018) 1700631.

- [6] S. Seropyan, I. Saikov, D. Andreev, G. Saikova, M. Alymov, Metals 11 (2021) 949.
- [7] C. Ji, Y. He, C.T. Wang, Y. He, Z. Guo, L. Guo, J. Non-Cryst. Solids 515 (2019) 149–156.
- [8] L. Wang, J. Liu, S. Li, X. Zhang, AIP Adv. 5 (2015) 117142.
- [9] Z. Zhang, H. Zhang, Y. Tang, L. Zhu, Y. Ye, S. Li, S. Bai, Mater. Des. 133 (2017) 435–443.
- [10] H. Ren, X. Liu, J. Ning, AIP Adv. 6 (2016) 115205.
- [11] H. Ren, X. Liu, J. Ning, Mater. Sci. Eng. A 660 (2016) 205–212.
- [12] A. Coverdill, C. Delaney, A. Jennrich, H. Krier, N.G. Glumac, J. Energ. Mater. 32 (2014) 135–145.
- [13] P. Luo, Z. Wang, C. Jiang, L. Mao, Q. Li, Mater. Des. 84 (2015) 72–78.
- [14] L. Wang, J. Jiang, M. Li, J. Men, S. Wang, Def. Technol. 17 (2021) 467–477.
- [15] L. Xing, X. Liu, Z. Cao, C. He, J. Liu, Mater. Sci. Eng. A 831 (2022) 142196.
- [16] B.B. Aydelotte, N.N. Thadhani, Mater. Sci. Eng. A 570 (2013) 164–171.
- [17] R. Wang, Y. Tang, S. Li, Y. Ai, Y. Li, B. Xiao, L. Zhu, X. Liu, S. Bai, J. Alloy. Compd. 825 (2020) 154099.
- [18] E.P. George, W.A. Curtin, C.C. Tasan, Acta Mater. 188 (2020) 435–474.
- [19] E.P. George, D. Raabe, R.O. Ritchie, Nat. Rev. Mater. 4 (2019) 515–534.
- [20] D.B. Miracle, O.N. Senkov, Acta Mater. 122 (2017) 448–511.
- [21] W. Zhang, P.K. Liaw, Y. Zhang, Sci. China Mater. 61 (2018) 2–22.
- [22] M.-H. Tsai, J.-W. Yeh, Mater. Res. Lett. 2 (2014) 107–123.
- [23] B. Cantor, Prog. Mater. Sci. 120 (2021) 100754.
- [24] W. Li, D. Xie, D. Li, Y. Zhang, Y. Gao, P.K. Liaw, Prog. Mater. Sci. 118 (2021) 100777.
- [25] Y. Darhovskiy, M. Mellincovsky, D. Baimel, A. Kuperman, Energy 231 (2021) 120789.
- [26] O.N. Senkov, J.M. Scott, S.V. Senkova, F. Meisenkothen, D.B. Miracle, C.F. Woodward, J. Mater. Sci. 47 (2012) 4062–4074.
- [27] O.N. Senkov, A.L. Pilchak, S.L. Semiatin, Metall. Mater. Trans. A 49 (2018) 2876–2892.
- [28] O.N. Senkov, S.L. Semiatin, J. Alloy. Compd. 649 (2015) 1110–1123.
- [29] V. Soni, O.N. Senkov, B. Gwalani, D.B. Miracle, R. Banerjee, Sci. Rep. 8 (2018) 8816.
- [30] H. Huang, Y. Wu, J. He, H. Wang, X. Liu, K. An, W. Wu, Z. Lu, Adv. Mater. 29 (2017) 1701678.
- [31] X. Fan, R. Li, X. Liu, Q. Liu, X. Tong, A. Li, S. Xu, H. Yang, P. Yu, G. Li, Mater. Sci. Eng. A 832 (2022) 142492.
- [32] X.S. Liu, R. Li, Y. Lu, Y.F. Zhang, P.F. Yu, G. Li, Mater. Sci. Eng. A 822 (2021) 141674.
- [33] S. Huang, W. Li, E. Holmström, L. Vitos, Sci. Rep. 8 (2018) 12576.
- [34] M. Wang, M.X. Huang, Acta Mater. 188 (2020) 551–559.
- [35] M.A. Meyers, Dynamic Behavior of Materials, Wiley, New York, 1994.
- [36] G.Z. Voyiadjis, F.H. Abed, Mech. Mater. 37 (2005) 355–378.
- [37] G. Dirras, H. Couque, L. Liliensten, A. Hecczel, D. Tingaud, J.-P. Couzinié, L. Perrière, J. Gubicza, I. Guillot, Mater. Charact. 111 (2016) 106–113.
- [38] S. Zhang, Z. Wang, H.J. Yang, J.W. Qiao, Z.H. Wang, Y.C. Wu, Intermetallics 121 (2020) 106699.
- [39] B. Schuh, B. Völker, J. Todt, N. Schell, L. Perrière, J. Li, J.P. Couzinié, A. Hohenwarter, Acta Mater. 142 (2018) 201–212.
- [40] Z. Li, S. Zhao, S.M. Alotaibi, Y. Liu, B. Wang, M.A. Meyers, Acta Mater. 151 (2018) 424–431.
- [41] P.G. Klemens, R.K. Williams, Int. Met. Rev. 31 (1986) 197–215.
- [42] J.E. Field, Acc. Chem. Res. 25 (1992) 489–496.
- [43] P. Kofstad, J. Common Met. 12 (1967) 449–464.
- [44] S. Sawada, J. Phys. Soc. Jpn. 11 (1956) 1237–1246.
- [45] J. Berkowitz, W.A. Chupka, M.G. Inghram, J. Chem. Phys. 27 (1957) 85–86.
- [46] O.G. Cervantes, J.D. Kuntz, A.E. Gash, Z.A. Munir, Combust. Flame 157 (2010) 2326–2332.
- [47] I.V. Roisman, K. Weber, A.L. Yarin, V. Hohler, M.B. Rubin, Int. J. Impact Eng. 22 (1999) 707–726.
- [48] R.L. Woodward, Int. J. Impact Eng. 18 (1996) 369–381.
- [49] C.E.A., Int. J. Impact Eng. 108 (2017) 3–26.
- [50] Z. Rosenberg, E. Marmor, M. Maysel, Int. J. Impact Eng. 10 (1990) 483–486.
- [51] L.S. Magness, Mech. Mater. 17 (1994) 147–154.
- [52] A. Tate, J. Mech. Phys. Solids 17 (1969) 141–150.
- [53] D.R. Christman, J.W. Gehring, J. Appl. Phys. 37 (1966) 1579–1587.
- [54] X.F. Liu, Z.L. Tian, X.F. Zhang, H.H. Chen, T.W. Liu, Y. Chen, Y.-J. Wang, L.-H. Dai, Acta Mater. 186 (2020) 257–266.
- [55] H. Chen, X. Zhang, L. Dai, C. Liu, W. Xiong, M. Tan, Def. Technol. (2021), doi:10.1016/j.dt.2021.06.001.
- [56] G. Birkhoff, D.P. MacDougall, E.M. Pugh, S.G. Taylor, J. Appl. Phys. 19 (1948) 563–582.